2012 IEEE International Conference on Robotics and Automation
RiverCentre, Saint Paul, Minnesota, USA
May 14-18, 2012

The Jacobs Robotics Approach to Object Recognition and Localization in the Context of the ICRA'11 Solutions in Perception Challenge

Narunas Vaskevicius Kaustubh Pathak Alexandru Ichim Andreas Birk

***Abstract*— In this paper, we give an overview of the Jacobs Robotics entry to the ICRA'11 Solutions in Perception Challenge. We present our multi-pronged strategy for object recognition and localization based on the integrated geometric and visual information available from the Kinect sensor. Firstly, the range image is over-segmented using an edge-detection algorithm and regions of interest are extracted based on a simple shape-analysis per segment. Then, these selected regions of the scene are matched with known objects using visual features and their distribution in 3D space. Finally, generated hypotheses about the positions of the objects are tested by back-projecting learned 3D models to the scene using estimated transformations and sensor model. Our method won the second place among eight competing algorithms, only marginally losing to the winner.**

I. Introduction

This paper gives an overview of the approach used by the Jacobs Robotics team in the ICRA 2011 Solutions in Perception Challenge. Object recognition has been long studied in general and it recently found quite some attention with respect to the use of combined RGB and depth information - especially in form of Kinect data [1], [2], [3], [4], [5]. Due to space limitations, we focus in this paper on the technical description of our methods and an in-depth discussion of the general state of the art is omitted; the literature references are hence limited to a minimum to point to the work on which we build upon and to indicate where we extend it.

The paper is organized in the following way. Firstly, we introduce our notation, used throughout the paper, in Sec. I-A. Then an overview of the object recognition system is given in Sec. II. The subsequent sections have detailed description of each of the introduced components and the underlying algorithms. The experimental setup and comprehensive benchmarking on two data-sets from ICRA 2011 Solutions in Perception Challenge is provided in Sec. VII. Finally, concluding remarks are presented in section Sec. VIII.

A. Notation

The notation used in this paper is summarized in Table I. In general, scalars are in normal lowercase letters, vectors in bold small letters, and matrices in bold capitals. For quantities resolved in different frames, we use the left superscript/subscript notation of [6]. Right subscripts are used for indexing or for denoting vector components.

Using this notation, the position vectors of the same physical point observed from two different frames $\mathcal{F}_i$ and $\mathcal{F}_j$ with their origins at O_i and O_j respectively, are related by

$$ {}^{i}\underline{\mathbf{p}} = {}^{i}_{j}\mathbf{T}\ {}^{j}\underline{\mathbf{p}}, \text{ where,} \tag{1a} $$

$$ {}^{i}_{j}\mathbf{T} \triangleq \begin{bmatrix} {}^{i}_{j}\mathbf{R} & {}^{i}_{j}\mathbf{t} \\ \mathbf{0}_3^{\mathsf{T}} & 1 \end{bmatrix}, \qquad {}^{i}_{j}\mathbf{t} \triangleq \overrightarrow{O_i O_j} \text{ resolved in } \mathcal{F}_i. \tag{1b} $$

Using $\simeq$ to show equality up to a positive scale-factor and the camera intrinsic parameter [7] matrix $\mathbf{C}$, the camera model is given by

$$ {}^{i}\underline{\mathbf{c}} \triangleq \mathbf{C}^{-1}\ {}^{i}\underline{\mathbf{m}}, \qquad {}^{i}\underline{\mathbf{c}} \simeq {}^{i}\mathbf{p}, \tag{2a} $$

$$ {}^{i}\underline{\mathbf{m}} \overset{(1)}{\simeq} \mathbf{C}\begin{bmatrix} {}^{i}_{j}\mathbf{R} & {}^{i}_{j}\mathbf{t} \end{bmatrix}\ {}^{j}\underline{\mathbf{p}}, \qquad {}^{i}\underline{\mathbf{c}} \simeq {}^{i}_{j}\mathbf{R}\ {}^{j}\mathbf{p} + {}^{i}_{j}\mathbf{t}, \tag{2b} $$

TABLE I
Notation

${}^{i}\mathbf{p} \in \mathbb{R}^3$	Position vector of a spatial point resolved in the reference frame $\mathcal{F}_i$.
${}^{i}\underline{\mathbf{p}} \in \mathbb{R}^4$	The homogeneous coordinates for ${}^{i}\mathbf{p}$.
${}^{i}\mathbf{M}$	Original image taken from camera-frame $\mathcal{F}_i$.
${}^{i}\mathbf{m} \in \mathbb{R}^2$	Image pixel coordinates of a point in an image taken from the camera-frame $\mathcal{F}_i$.
${}^{i}\underline{\mathbf{m}} \in \mathbb{R}^3$	The homogeneous coordinates for ${}^{i}\mathbf{m}$.
${}^{i}\mathbf{c} \in \mathbb{R}^2$	Normalized camera coordinates of a point in an image taken from camera-frame $\mathcal{F}_i$.
${}^{i}\underline{\mathbf{c}} \in \mathbb{R}^3$	The homogeneous coordinates for ${}^{i}\mathbf{c}$.

II. Design of the Recognition System

The workflow of the recognition system for detecting and localizing objects from a single view-point is depicted in Fig. 1. The recognition is done by combining texture information obtained from a color-image with geometric properties of the scene observed in a depth-image. For that, object database of point-cloud based 3D models with visual and shape cues is created during the training phase (Sec. III). These models are then used to generate hypotheses about the objects in the observed environment. This is done in the following way.

Segmentation. Firstly, the geometric properties of sensor data are examined by dividing range-image into regions of smooth surface patches. This is achieved by the algorithm described in Sec. IV. A very important aspect of our approach is the over-segmentation of the scene. In other words, there is no commonly used assumption that a segment must represent the whole object, which usually limits recognition to environments with well-separated objects on an easily detectable support surface, such as a table-top. On the contrary, finding smooth sub-segments of the objects is a plausible task even in cluttered scenes.

Regions of Interest. As described in Sec. IV-A the segmentation result can be used to filter out large parts of the sensor data. Shape properties of a patch can be compared against those of the learned models to check if the segment could possibly be a part of any object from the database. Effectively, large planar surfaces (e.g. walls, floor, table-tops etc.) or other geometrically inconsistent segments

The authors are with the Dept. of EECS, Jacobs University Bremen, 28751 Bremen, Germany. {n.vaskevicius, k.pathak, a.birk}@jacobs-university.de

The research leading to the results presented here has received funding from the European Community's Seventh Framework Programme (EU FP7 ICT-2) within the project "Cognitive Robot for Automation Logistics Processes (RobLog)".

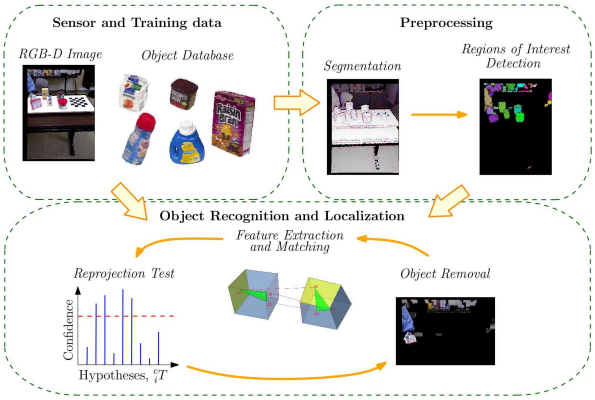

Fig. 1. Object recognition and localization in a single RGB-D frame

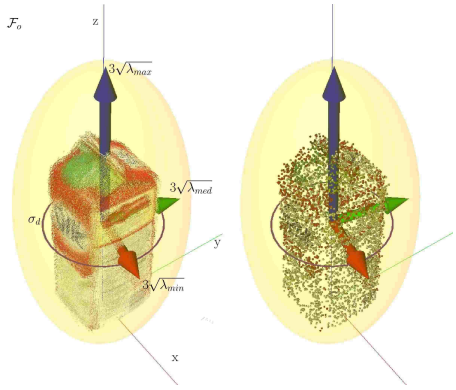

Fig. 2. A model of the Silk Original soy milk carton on the left and the corresponding SURF feature locations on the right.

are removed and not considered in the recognition process. The detection of regions of interest significantly reduces search space for recognition and localization algorithm, but is completely optional.

Feature Extraction and Matching. After the preprocessing step, we combine the regions of interest into a global mask and use it for extraction of texture features (e.g. Speeded Up Robust Features (SURF) [8], [9], the Scale Invariant Feature Transform (SIFT) [10], etc.). As explained in Sec. V each feature descriptor vector is associated with a 3D pose with respect to the range sensor. Then, the hypothesis about the best position in the scene is generated for each object using random sample consensus (RANSAC) [11] based feature-matching with 3D geometric constraints (Algorithm 2).

Testing Hypotheses. The transforms computed by the matching algorithm are used to re-project the models of the objects. Color and range consistency tests (Sec. VI) are then used to filter out false-positives. Objects with high consistency scores are considered to be recognized and their corresponding regions of interest are removed from the scene. Detection is then re-iterated on the remaining segments to handle multiple instances of the same object.

III. 3D Models of Real-World Objects

This section describes the model used by the recognition system to represent real-world ojects.

We use a set of 3D points sampled from the object's surface paired with the colors at their locations to model the shape and appearance of the real-world instance:

$$\mathcal{P} \triangleq \mathbb{P} \times \mathbb{C} = \left\{ \langle \mathbf{p}, \mathbf{c} \rangle \mid \mathbf{p} \in \mathbb{P} \triangleq \mathbb{R}^3, \mathbf{c} \in \mathbb{C} \right\}. \tag{3}$$

Here $\mathbb{C}$ denotes a color space e.g. *RGB*, *CIE* $L^*A^*B^*$, etc.

The following quantities are calculated using Principal Component Analysis (PCA) on the point-cloud $\mathbb{P}$ to describe the dimensions of the object:

$$\sigma_{min} \triangleq 2 \cdot 3\sqrt{\lambda_{min}}, \qquad \sigma_{max} \triangleq 2 \cdot 3\sqrt{\lambda_{max}}, \tag{4a}$$

$$\sigma_d \triangleq \frac{1}{2} \cdot 6\sqrt{\lambda_{med} + \lambda_{min}}, \tag{4b}$$

where, $\lambda_{max}, \lambda_{med}, \lambda_{min}$ are sorted eigenvalues of the covariance matrix calculated during PCA. σ_{min} and σ_{max} are respectively the minimum and maximum extent of the object. The PCA on the set $\mathbb{P}$ can be viewed as an ellipsoidal approximation of the object's shape. Thus, the diameter σ_d of gyration of the ellipsoid about the principle PCA axis can be interpreted as the approximate diameter of the object. As described in Sec. IV-A, these three values $\Sigma \triangleq \{\sigma_{min}, \sigma_{max}, \sigma_d\}$ are used to find regions of interest during the recognition phase.

In addition to the geometric properties, the model also contains a set of local invariant texture features [12].

$$\mathcal{D} \triangleq \mathbb{D} \times \mathbb{P} = \left\{ \langle \mathbf{d}^{(n)}, \mathbf{p} \rangle \mid \mathbf{d}^{(n)} \in \mathbb{R}^n, \mathbf{p} \in \mathbb{P} \right\} \tag{5}$$

The n-dimensional feature descriptor vectors $\mathbf{d}^{(n)}$ are coupled with their locations on the object to aid feature matching and localization steps (Sec. V).

Thus, the object model is defined by the 3-tuple $\langle \mathcal{P}, \mathcal{D}, \Sigma \rangle$. The example of a model for one of the objects from Solutions in Perception Challenge data-set is illustrated in Fig. 2. The transparent ellipsoid represents the three-sigma PCA approximation of the object's shape. Its minor, medial and major axes are demonstrated respectively by red, green and blue arrows. The purple circle surrounding the object has the radius of σ_d.

IV. Segmentation

Segmentation is the process of dividing a range-image into connected components or segments, each of which is a smooth surface patch which is separated from its neighbors by jump or crease edges. A jump edge is formed when two neighboring segments have a physical separation causing a C_0 discontinuity in the range values. A crease edge, on the other hand, is a C_1 range-discontinuity between segments which physically touch along the edge. Each segment represents a facet – not necessarily planar – of an object in the scene.

The segmentation algorithm devised by us is an extension of that presented in [13] and is summarized in Algorithm 1. A scan-line in a range-image is defined as either a row, a column, or a diagonal (ascending or descending) of the range-image. Each scan-line is processed separately, and is split into curve-segments using the method of [14], also known as the Ramer-Douglas-Peucker algorithm. Essentially, a scan-line can be considered as a *piece-wise* smooth mapping from the scan-line pixel-index $x \in \mathbb{Z}$ to the range or depth value $z \in \mathbb{R}$. Algorithm 1 is used to find this mapping: in other words, it finds the edge-points which separate the scan-line into sub-segments, each of which is a smooth function $z = f_i(x)$. Two main functions of the Algorithm 1 are `Fit` and `Split`.

In the `Fit` function, a polynomial is fitted to a given sub-segment of a scan-line. This can be done in several ways.

- *Simple linear (SL) or quadratic (SQ):* For the linear version, the first and last points of the sub-segment are used to fit a

Algorithm 1: Scan-Line Edge-Detection

Input: A set C of scan-lines: rows, columns, or diagonals of a range-image.
Output: A set of smooth sub-segments $\mathcal{S}_f$ of all scan-lines in C.
forall the $c \in C$ **do**
  From scan-line c, form an initial stack $\mathcal{S}_c$ of connected valid-range segments, separated by invalid ranges;
  while $|\mathcal{S}_c| \neq 0$ **do**
    $s \leftarrow \mathcal{S}_c$.Pop() ;
    Fit(s) ;
    if Split(s, split-index) **then**
      left-segm $\leftarrow$ s[0 . . . split-index] ;
      right-segm $\leftarrow$ s[split-index . . . end-index] ;
      $\mathcal{S}_c$.Push(left-segm), $\mathcal{S}_c$.Push(right-segm) ;
      Mark edge-point s[split-index] ;
    else
      $\mathcal{S}_f$.Push(s) ;
    end
  end
end

unique line; for the quadratic version, the mid-point is also added to fit a unique quadratic polynomial.

- *Least-squares linear (LSL) or quadratic (LSQ):* All points in the sub-segment are considered, and a linear or a quadratic polynomial is fitted using a standard least-squares method, minimizing the sum of algebraic residuals.
- *Adaptive (AD):* This is our extension of the algorithm. Recall that for a least-squares model-fitting – assuming a constant known Gaussian noise with variance σ^2 in all samples – the Akaike Information Criterion (AIC), and its corrected version for small sample-size (AICc) [15], for the model-fit may be defined as

$$\mathrm{AIC}(\{r_i\}, K, N) = 2K + \frac{1}{\sigma^2}\sum_{i=1}^{N} r_i^2 - 2C, \tag{6}$$

$$\mathrm{AICc} = \mathrm{AIC} + \frac{2K(K+1)}{(N-K-1)}, \tag{7}$$

where, K is the number of parameters in the model, C is a constant, depending only on the known parameter σ^2, N is the number of samples, and r_i is the least-squares fitting residual for the sample i.
The adaptive strategy consists of fitting a least-squares linear polynomial ($K = 2$) on the sub-segment, followed by fitting a least-squares quadratic polynomial ($K = 3$), and selecting the one with the lower value of AICc.

The function `Split` consists of checking if a sub-segment s of a scan-line c can be spit further into subsegments, and if so, at which x. This x value is denoted by `split-index`. The function returns `true`, if the splitting is to take place. For a sub-segment to be considered for further splitting, it should have at least $\lambda_{\min}$ points. There are two main splitting strategies.

- *Maximum residual (MR):* The candidate splitting point in the sub-segment is the one with the maximum residual r_m from the fitted polynomial. The splitting is done if $r_m > \epsilon$, where ϵ depends on the noise level of the data. This strategy has been followed in [13]. Although in [13] both SQ and LSQ were used for fitting, they did not discuss an important problem which often arises when using LSQ with MR, namely, that many times the candidate split-point turns out to be the very first point of the sub-segment. This does not occur when using SQ with MR as the residual at the end-points is explicitly zero. We have hence concluded that LSQ+MR is not a good combination.
- *Minimum AICc (MAIC):* This is our extension of the algorithm. For a sub-segment s, after doing an adaptive fitting, all points where the residual achieves a local maximum are considered potential splitting points. We consider all of these potential points in turn, and compute the decrease in AICc on hypothetically splitting the segment at that point. If none of the candidates lead to a decrease in AICc as compared to the un-split segment, no splitting is performed; else, the candidate which leads to the most decrease is selected as the splitting point. Note that fitting for all subsegments is done adaptively, i.e. their number of parameters is adaptively selected.

TABLE II
MAIN EDGE-DETECTION MODES.

Mode	Fitting	Splitting	Time (s)
Simple-Linear	SL	MR	2.3
Simple-Quadratic	SQ	MR	2.3
LS-AICC	AD	MAIC	13.1
LS-Mixed	SQ+AD	MR+MAIC	3.5

Based on the above description, and after doing some experimentation, we came up with four combined strategies for comparison, as listed in Table II. The runtime listed is for the processing of the whole image, i.e. for all rows, columns, and diagonals. In mode LS-Mixed, fitting and splitting strategies are based on those of Simple-Quadratic initially; after the segment size reduces below $\lambda_{\min} f_{\mathrm{mixed}}$, the strategy switches to that of LS-AICC. This strategy is thus a compromise in the trade-off between quality and computation time, and hence is our default strategy due to its good results. Please refer to Fig. 3(b) for the quality of edge-detection on range images collected using the Kinect sensor with the parameters $\epsilon = \sigma = 0.015$ m, $\lambda_{\min} = 4$ and $f_{\mathrm{mixed}} = 12$. The switching of strategies was done when a sub-segment size had reduced to 48 pixels.

A. Filtering-out and Smoothing Objects of Interest

The edge-points in the left sub-figures of Fig. 3 do not yet form closed boundaries of the object surface patches they demarcate. To achieve this, certain morphological transforms, as implemented in OpenCV [16], are applied, which is also done in [13]. In particular, an erosion with a kernel size of 5 followed by a dilation with a kernel size of 3 gave satisfatory separation of connected components for the 3D sensor employed.

From the training phase, the algorithm has good estimates of the dimensions of the objects it is looking for. The sizes of all trained objects are used to come up with minimum and maximum thresholds, which can be used to filter out extraneous objects and the background. Any predominantly planar objects which are significantly bigger than the thresholds are filtered out first. This is accomplished by first applying a distance-transform (DST implementation in OpenCV) on the edge-points image: the peaks of the resulting image give points which are far away from the edges and hence are good seeds to grow planar patches from. A region-growing algorithm [17] was used to grow planar patches. All dominant planar patches, which cannot possibly be part of an object of interest due to their size, are filtered out irrespective of their orientation. This typically removes walls, table-tops, etc. and makes subsequent processing much simpler.

After removing large planes, a connected-components algorithm

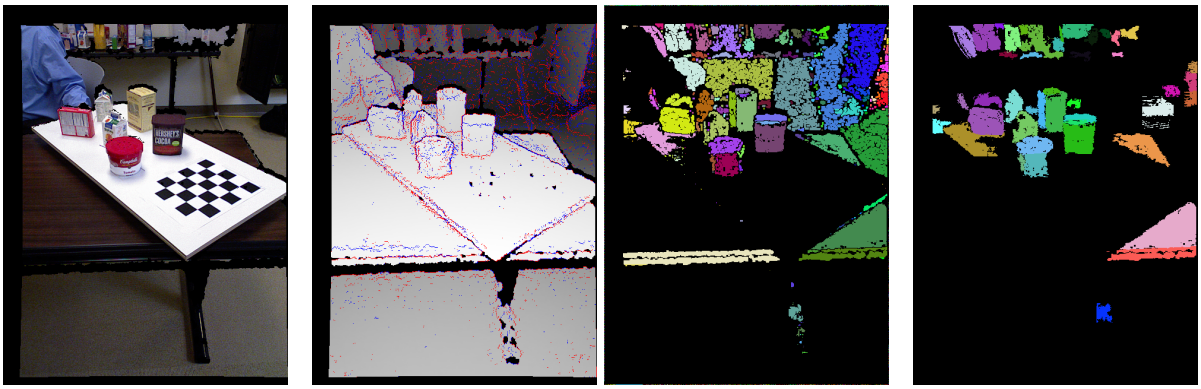

(a) The original colored range-image.

(b) Mode LS-Mixed.

(c) The final smoothened filtered out objects of interest.

Fig. 3. Results of segmentation for one of the example test scenes. The left image in Fig. 3(b) shows the found edge-points using LS-Mixed mode. The point-color denotes the convex/concave categorization of the edge w.r.t the view point. The images on the right show the color connected-components representing object patches. Before running the connected-components algorithm a morphological transform was applied to clearly separate the components.

[18] is run to find potential object components as shown in the right side sub-figure of Fig. 3(b), where each component is given a unique color. To these remaining connected components, Principal Component Analysis (PCA) is performed and components with dimensions not falling within the limits determined during the training phase are removed. Finally, we expand and smoothen the remaining components. This is done by fitting a 3D quadric surface [19] on a found component and testing its neighboring points to see if they satisfy the quadric equation within some bounds: if they do, they are made part of the component. This results in filling-in of holes and smoothing of the components which now represent object surface patches— these are shown in Fig. 3(c). Interestingly, the time taken for removing large planes, finding connected-components, and filtering-out objects of interest, followed by smoothing them, was 0.13 sec., which is a fraction of the time required for scan-line edge-detection (Table II, mode LS-Mixed).

V. Feature Extraction and Matching

After the segmentation step the regions of interest are combined into a global mask. Then a standard feature extraction pipeline is applied on this image mask. Firstly, a set of distinctive keypoints is detected and then the region content around each of the keypoints is summarized in feature descriptor vectors. Instead of keeping keypoints defined in image coordinates, the corresponding 3D positions resolved in the object frame are calculated using relations in equation (2b). The 3D keypoint-descriptor pairs define the set $\mathcal{D}_s$. Then for all objects o_i in model data-base, their feature-set $\mathcal{D}_i$ is matched against feature-set in the scene using Algorithm 2.

The matching algorithm starts by finding a set of feature correspondence pairs between the object and the scene - `FindFeatureCorrespondences`. For each feature vector $\tau_j.\mathbf{d}^{(n)}$, $\tau_j \in \mathcal{D}_i$ the nearest neighbor $\tau^\star.\mathbf{d}^{(n)}$, $\tau^\star \in \mathcal{D}_s$ is found using Euclidean distance in the feature space. If distance between features is small enough i.e. $\|\tau_j.\mathbf{d}^{(n)} - \tau^\star.\mathbf{d}^{(n)}\| < \Delta_f$, then the pair $\langle \tau_j, \tau^\star \rangle$ is added to the list of potential correspondences - $\mathcal{T}_f$. Note that the uniqueness of the closest feature is not tested. This is usually done using the ratio between the distances to the two closest features. We have tried different strategies and the results were better when the additional filtering by the ratio was not applied. Using only the nearest features increases both the number of correct and false correspondences. The higher rate of the false correspondence pairs is acceptable since they are effectively eliminated by the 3D geometric constraints during the matching algorithm. The full set of correspondences $\mathcal{T}_f$ is then sorted by the correspondence distance and only α% with the smallest distances are kept for the outer loop.

Algorithm 2: RANSAC Based Feature Matching

Input: $\mathcal{D}_s$, $\mathcal{D}_i$
Output: ${}^s_i\mathbf{T}$ and c_{max} - size of the maximum consensus set.

```
T_f ← FindFeatureCorrespondences(D_s, D_i);
T_f ← Sort(T_f);
T_α ← Filter(T_f, α);
forall the ⟨ˢτ₁, ᵒτ₁⟩ ∈ T_α do
    T_2 ← FindConsistent(⟨ˢτ₁, ᵒτ₁⟩, T_f);
    T_β ← Filter(T_2, β);
    forall the ⟨ˢτ₂, ᵒτ₂⟩ ∈ T_β do
        T_3 ← FindConsistent(⟨ˢτ₂, ᵒτ₂⟩, T_β);
        ⟨ˢ_iT_j, c_j⟩ ← RANSAC(T_3, n_r);
        if c_j > c_n then
            c_n ← c_j;
            ˢ_iT ← ˢ_iT_j;
        end
    end
end
```

For each element $\langle {}^s\tau_1, {}^o\tau_1 \rangle \in \mathcal{T}_\alpha$ a set of geometrically consistent correspondences is constructed. Two feature pairs $\langle {}^s\tau_1, {}^o\tau_1 \rangle, \langle {}^s\tau_2, {}^o\tau_2 \rangle \in \mathcal{D}_s \times \mathcal{D}_o$ are geometrically consistent if the following equation is satisfied

$$\left\| {}^s\tau_2.\mathbf{p} - {}^s\tau_1.\mathbf{p} \right\| = \left\| {}^o\tau_2.\mathbf{p} - {}^o\tau_1.\mathbf{p} \right\|. \tag{8}$$

This first test is based on the observation that if the object in the scene and its model have the same scale then the layout of the features with respect to each other is preserved. Thus the distances from all model features ${}^o\tau_j$ to a fixed feature ${}^o\tau_1$ are the same as the distances of their correct counterparts in the scene ${}^s\tau_j$ to the corresponding fixed feature ${}^s\tau_1$.

After keeping the best β% correspondences from the $\mathcal{T}_2$ set the inner loop fixes the second correspondence pair - $\langle {}^s\tau_2, {}^o\tau_2 \rangle \in \mathcal{T}_\beta$. The additional constraint introduced by the second pair allows us to further reduce the number of candidate correspondences. The

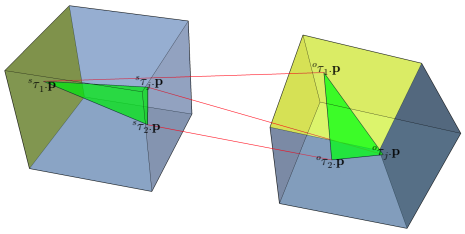

Fig. 4. If the objects in the scene and their models are of the same scale then the triangles formed by three correct correspondences are congruent

$\mathcal{T}_3$ is formed of the features geometrically consistent with the fixed correspondences. The geometric constraints introduced by two fixed correspondence pairs are illustrated in Fig. 4. For any correct correspondence $\langle {}^s\tau_j, {}^o\tau_j \rangle \in \mathcal{T}_\beta$ the triangles $\langle {}^s\tau_1.\mathbf{p}, {}^s\tau_2.\mathbf{p}, {}^s\tau_j.\mathbf{p} \rangle$ and $\langle {}^o\tau_1.\mathbf{p}, {}^o\tau_2.\mathbf{p}, {}^o\tau_j.\mathbf{p} \rangle$ have to be congruent.

Though heavily pruned, the set $\mathcal{T}_3 \subset \mathcal{T}_f$ still might have outliers due to the sensor noise and approximation by the parameter Δ_f. Also, since only two correspondences were fixed, there still might be geometrically inconsistent correspondences. To address these problems a standard RANSAC algorithm [11] is applied on the set $\mathcal{T}_3$. Three correspondences are randomly selected and the transformation ${}^s_o\mathbf{T}$ between the model and the scene is estimated using [20]. Then the consesus set is created: a feature pair is considered consistent if

$$\left\| {}^s\tau_j.\mathbf{p} - {}^s_o\mathbf{T}\, {}^o\tau_j.\mathbf{p} \right\| \leq \Delta_d. \tag{9}$$

After n_r iterations all correspondences in the largest consensus set are used to recalculate the final estimate ${}^s_o\mathbf{T}$. The rate of outliers in the set $\mathcal{T}_3$ is very low. In most of the cases the largest consensus set is equal to $\mathcal{T}_3$, therefore only few iterations are needed. As specified in Table III we have used $n_r = 100$.

The final result of the Algorithm 2 is the transformation calculated using the largest consensus set obtained by fixing different correspondences in the loops. The worst case computational complexity for the object with feature set $\mathcal{D}$ is $O(|\mathcal{D}|^3)$. However, in practice, due to geometric constraints and parameters α, β and Δ_f, the matching can be used in real-time applications even with feature-sets of size up to 10^5.

VI. Reprojection Test

The matching algorithm described in the previous section is applied to all the models $o_j, j = 1 \ldots n$ in the training database. Thus for each object an estimate of its best location in the scene ${}^s_j\mathbf{T}$ is determined based on the largest consensus set with size c_j. In many cases, if the object is not in the scene, even the minimum consensus set (of size 3) is not constructed due to the small initial correspondence set and geometric constraints. However the local feature descriptors and their configuration in 3D space are not always enough to distinguish objects uniquely; therefore false positives have to be eliminated.

The size of the consensus set could already be used as the criteria for discarding objects not present in the scene, but for which the location estimate has been generated. Unfortunately, the variation in the number of features per model is quite large. Less textured objects would have always small consensus sets even though they are present in the scene, whereas highly textured objects would usually have a larger subset of features which would be consistent with some part of the scene. Therefore, more complicated tests are needed for checking the hypotheses. For this, we perform a simulation of data collection using a sensor model and the hypotheses generated by Algorithm 2. The consistency between the simulated data and the real measurements is then checked for the identification of the correct hypotheses.

As described in Sec. III, the object model o_j is defined by the three-tuple $\langle \mathcal{P}_j, \mathcal{D}_j, \Sigma_j \rangle$. The set of colored points $\mathcal{P}_j$ can be transformed to the sensor frame using the hypothesis about its location - ${}^s_j\mathbf{T}$. Using the camera model Eq. (**??**), these points can be projected onto the image plane. We have used depth-buffer for projecting only those parts of the object which are visible from the position of the sensor. Thus for each object o_j in the data-base, an RGB-D image ${}^s\mathbf{M}_j$ is generated.

$$ {}^s\mathbf{M}_j({}^s\mathbf{m}) = \underset{{}^s\tau \in {}^s\mathcal{P}({}^s\mathbf{m})}{\mathbf{argmin}} \|{}^s\tau.\mathbf{p}\|, \tag{10}$$

$$ {}^s\mathcal{P}({}^s\mathbf{m}) \triangleq \left\{ {}^s\tau \triangleq \langle {}^s_j\mathbf{T}\, {}^j\tau.\mathbf{p}, {}^j\tau.\mathbf{c} \rangle \mid {}^s\underline{\mathbf{m}} \simeq \mathbf{C}\, {}^s\tau.\mathbf{p} \right\} \tag{11}$$

Let $\mathbb{M}_j \triangleq \{ {}^s\mathbf{m} \,|\, \exists {}^j\tau \in {}^j\mathcal{P} : {}^s\underline{\mathbf{m}} \simeq \mathbf{C}\, {}^s_j\mathbf{T}\, {}^j\tau.\mathbf{p} \}$ be a set of discrete image coordinates obtained by projecting object model o_j. Also we denote $\mathcal{S} = \{\mathbb{S}_1, \mathbb{S}_2, \ldots \mathbb{S}_n\}$ to be a set of regions of interests obtained after the segmentation described in Sec. IV. Each of the regions is defined by a set of image coordinates. Then the following quantities are used to determine consistency between real and modeled data.

$$ \mathbf{s}_d \triangleq \frac{\sum_{\mathbf{m} \in \mathbb{M}_j} \mathbf{1}_d\{\mathbf{m}, {}^s\mathbf{M}_j(\mathbf{m})\}}{|\mathbb{M}_j|} \tag{12}$$

$$ \mathbf{s}_c \triangleq \frac{\sum_{\mathbf{m} \in \mathbb{M}_j} \mathbf{1}_c\{\mathbf{m}, {}^s\mathbf{M}_j(\mathbf{m})\}}{|\mathbb{M}_j|} \tag{13}$$

$$ f(\mathbb{S}) \triangleq \sum_{\mathbf{m} \in \mathbb{M}_j \cap \mathbb{S}} \mathbf{1}_d\{\mathbf{m}, {}^s\mathbf{M}_j(\mathbf{m})\} \wedge \mathbf{1}_c\{\mathbf{m}, {}^s\mathbf{M}_j(\mathbf{m})\}$$

$$ \mathbf{s}_o \triangleq \frac{f(\mathbb{S}^\star)}{|\mathbb{S}^\star|}, \quad \mathbb{S}^\star \triangleq \underset{\mathbb{S} \in \mathcal{S}}{\mathbf{argmax}}\, f(\mathbb{S}) \tag{14}$$

The quantities defined in equations (12) and (13) respectively are distance and color consistency measures. For each pixel $\mathbf{m}$ in the mask $\mathbb{M}_j$ of the projected model consistency is checked using indicator functions $\mathbf{1}_d\{\cdot\}$ and $\mathbf{1}_c\{\cdot\}$. The depth similarity at pixel $\mathbf{m}$ is evaluated by comparing the range values at the same pixel in the simulated and the real RGB-D images:

$$ \mathbf{1}_d(\mathbf{m}, \tau) \triangleq \begin{cases} 1, & |\|{}^s\mathbf{M}(\mathbf{m}).\mathbf{p}\| - \|\tau.\mathbf{p}\|| < \varepsilon_d \\ 0, & \text{else.} \end{cases} \tag{15}$$

Color consistency is checked using a small window of size $2w + 1$ around pixel $\mathbf{m}$ in the real range image:

$$ \mathbf{1}_c(\mathbf{m}, \tau) \triangleq \begin{cases} 1, & \exists \mathbf{b} \in \mathbb{B}_w(\mathbf{m}) \colon \|{}^s\mathbf{M}(\mathbf{b}).\mathbf{c} - \tau.\mathbf{c}\|_c < \varepsilon_c \\ 0, & \text{else} \end{cases},$$

$$ \mathbb{B}_w(\mathbf{m}) \triangleq \{\mathbf{b} \,|\, |\mathbf{m}_u - \mathbf{b}_u| \leq w \wedge |\mathbf{m}_v - \mathbf{b}_v| \leq w\}. \tag{16}$$

Where, $\| \cdot \|_c$ is a color similarity metric. We have used *CIE* $L^*A^*B^*$ space where the perceptual difference between colors can be approximated by the Euclidean distance between the color vectors.

As it has already been discussed segments $\mathbb{S} \in \mathcal{S}$ are assumed to be subsegments of the objects, i.e. we assume over-segmentation. If the hypothesis about the object's location is correct then there must exist a segment with high consistency $\mathbb{S}^\star$ in the overlap between reprojected model and the segments in the real image $\{\mathbb{S} \in \mathcal{S} | \mathbb{M} \cap \mathbb{S} \neq \emptyset\}$. This requirement is expressed in equation (14), where function $f(\cdot)$ measures overlap consistency by comparing colors and ranges between simulated and real data. Using this function we can calculate the last quantity $\mathbf{s}_o$ needed for the consistency test. It measures coverage rate of the segment with the highest consistent overlap.

Fig. 5. A snapshot of all 35 objects from Willow Garage data-set on the left and a textured manufacturing part from NIST collection on the right [21]

Based on definitions (12), (13) and (14) the final consistency test is done using the following inequality.

$$(w_c \cdot \mathbf{s}_c + (1 - w_c) \cdot \mathbf{s}_d) \cdot \mathbf{s}_o \geq \theta_c, \tag{17}$$

where scalar $0 \leq w_c \leq 1$ is the weight factor for the color consistency measure and the threshold $0 \leq \theta_c \leq 1$ is the lowest allowed total consistency for the hypothesis to be considered correct. Thus, if the inequality (17) holds then the object o_j is considered to be in the scene at location ${}^s_j\mathbf{T}$. If there are at least two objects satisfying inequality (17), but having the same segment $\mathbb{S}^\star$ as the best overlaping region then only the object with the highest total conistency is considered to be detected.

So far we have described how to detect single instance of an object, however there might be multiple occurences of the same object in the scene. For detecting other instances of the same object we first remove corresponding segments of the recognized objects and then repeat the matching and reprojection steps with the remaining segments and objects with the total consistency higher than $\theta_c/2$. These steps are re-iterated until no more objects are detected.

VII. Experiments and Benchmarking

The approach described in the previous sections has been tested in a context of Solutions in Perception Challenge at International Conference on Robotics and Automation 2011 [21]. This was the first competition and it concentrated on the recognition and localization in 3D of textured objects at close range (approximately within 2 meters). The challenge made use of Kinect sensor which is able to produce RGB-D image at one mega-pixel resolution.

The data used for the challenge consisted of two data-sets totaling 50 objects. The first set, henceforth WG data-set, of 35 common household objects Fig. 5 was provided by researchers from Willow Garage before the competition. It contained extensive training sequences for each of the objects and example test scenarios with multiple objects per scene. The second data-set, henceforth NIST data-set, containing 15 objects was hidden from the participants to test robustness and generality of the developed algorithms. It comprised of textured manufacturing parts. Only single representitive example was available to the contestants before the testing phase of the competition. A picture of a typical object from the NIST data-set is shown in Fig. 5 on the right-hand side.

The recognition software developed by the participants had to be submitted to the competition committee. The algorithms were then trained and tested on their servers using before undisclosed data-sets containing one or more trained objects per frame. The test sequence with objects from WG data-set comprised of 176 frames with 434 recognizable objects in total. The NIST data-set had 831 object instances distributed over 399 frames. Full data was published after the challenge and is available online [21].

TABLE III

Values of the main algorithm parameters used for the competition

Parameters	Description	Values
Δ_f, Δ_d	Feature and distance similarity thresholds	1.0, 15 mm
n_r, α	Feature matching parameters	100, 0.1
w, w_c, θ_c	Reprojection parameters	4, 0.6, 0.4

The performance of the algorithms was evaluated at each frame using combinatorial scoring function based on the recognition rate and localization precision. The recognition score was dependant on the number of correct detections (true positives), incorrect detections (false positives) and undetected objects (false negatives), whereas localization score linearly decreased with increasing deviation of the pose estimate from the ground-truth. The detailed definitions of the contributing terms can be found in [21]. The final score of a team was expressed as percentage of the maximum possible score over all frames.

There are several implementation details to be mentioned before proceeding to the results. Firstly, object models Sec. III were created using the training data provided by the committee of the competition. It was recorded using Kinect sensor and Robot Operating System (ROS) [22]. Each of the textured objects was scanned from different view-points using rotating support and fiducial for estimation of the object-camera relation. The raw data had to be further processed to create models required by our algorithm. This included object segmentation, extraction of local invariant features, registration and some post-processing tasks. As the type of visual features we have chosen SURF with dimension $n = 128$. We have used OpenCV implementation for detecting key-points and computing descriptor vectors. The algorithm was optimized to produce the best performance within allowed time limit - 15 s. per frame.

Using the parameters listed in Table III the algorithm achieved the best score among all participants - 82.2% (682.61/831) on NIST data-set and the second result 50.6% (219.94/434) on Willow Garage data-set. The final combined score 66.41% took the second place behind the best score 68.78% achieved by the team from UC Berkeley. The number of true positives, false negatives, false positives, and the accuracy of position estimates were respectively 750, 81, 2, 86% for NIST and 301, 133, 50, 75.4% for WG test sets. Note that only true positives are included in the calculation of the localization accuracy. Further details on the competition results can be found in [21].

The final decision about the presence of an object instance in the scene is done using the reprojection parameter θ_c. Therefore more detailed analysis of the algorithm's sensitivity to the variations of the decision threshold is depicted in Fig. 6.

VIII. Conclusions

In this work we have presented an approach to object recognition and localization using visual and geometric cues available from RGB-D data. In addition to aiding the standard pipeline of visual object recogntion with depth information we have extended segmentation algorithm [13] to achieve better performance. As it already was emphasized the parameters of the edge-detection algorithm were set to achieve over-segmentation. Finding sub-segments of the objects does not require strong assumptions about the environment and as it was shown in this paper it can be applied in many stages of the object recognition process. One of them is reprojection test which was introduced by us to test the hypotheses about the objects present in the scene.

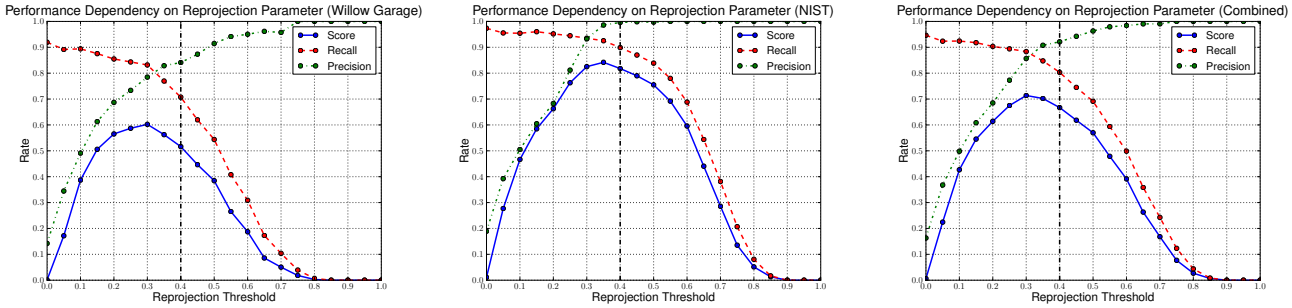

j

(a) Precision, recall, and score dependency on θ_c respectively for WG, NIST and combined data-sets

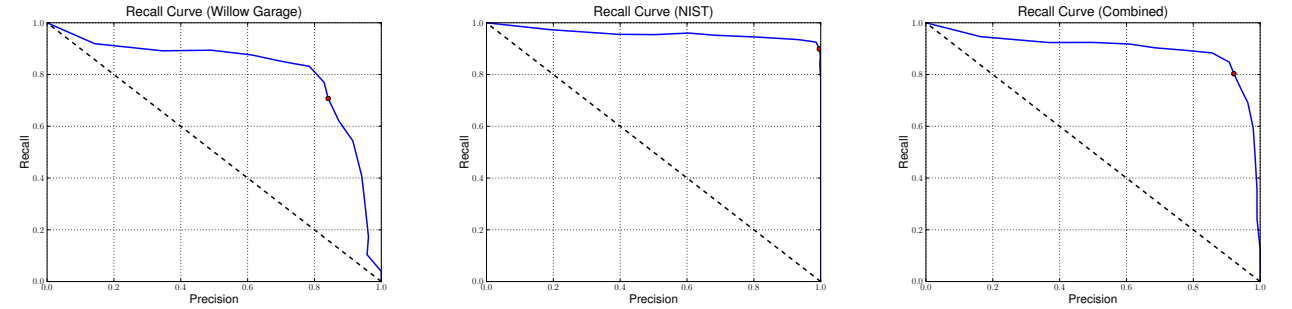

(b) Precision-recall curves for WG, NIST and combined data-sets

Fig. 6. Score dependency on the reprojection parameter θ_c and related precision-recall curves. The dashed vertical lines and the red circles indicate the parameter value $\theta_c = 0.4$ used for the competition.

The algorithm showed a good performance among eight entries to the Solutions In Perception Challenge by achieving the second best result, 66.41% of the maximum score, with only 2.37% difference from the first place.

References

[1] K. Lai, L. Bo, X. Ren, and D. Fox, "Sparse distance learning for object recognition combining rgb and depth information," in *Robotics and Automation (ICRA), 2011 IEEE International Conference on*, 2011, pp. 4007–4013.

[2] L. Bo, K. Lai, X. Ren, and D. Fox, "Object recognition with hierarchical kernel descriptors," in *Computer Vision and Pattern Recognition (CVPR), 2011 IEEE Conference on*, 2011, pp. 1729–1736.

[3] K. Lai, L. Bo, X. Ren, and D. Fox, "A large-scale hierarchical multi-view rgb-d object dataset," in *Robotics and Automation (ICRA), 2011 IEEE International Conference on*, 2011, pp. 1817–1824.

[4] N. Silberman and R. Fergus, "Indoor scene segmentation using a structured light sensor," 2011.

[5] J. Knopp, M. Prasad, and L. V. Gool, "Scene cut: Class-specific object detection and segmentation in 3d scenes," in *3D Imaging, Modeling, Processing, Visualization and Transmission (3DIMPVT), 2011 International Conference on*, 2011, pp. 180–187.

[6] J. J. Craig, *Introduction to robotics – Mechanics and control*. Prentice Hall, 2005.

[7] R. Elias, "Projective geometry for three-dimensional computer vision," in *Seventh World Multiconference on Systemics, Cybernetics and Informatics*, vol. v, Orlando, Florida, 2003, pp. 99–104.

[8] H. Bay, A. Ess, T. Tuytelaars, and L. Van Gool, "Speeded-up robust features (surf)," *Computer Vision and Image Understanding*, vol. 110, no. 3, pp. 346–359, 2008.

[9] H. Bay, T. Tuytelaars, and L. Van Gool, *SURF: Speeded Up Robust Features Computer Vision ECCV 2006*, ser. Lecture Notes in Computer Science. Springer Berlin / Heidelberg, 2006, vol. 3951, pp. 404–417.

[10] D. G. Lowe, "Distinctive image features from scale-invariant keypoints," *International Journal of Computer Vision*, vol. 60, no. 2, pp. 91–110, 2004.

[11] M. A. Fischler and R. C. Bolles, "Random sample consensus: a paradigm for model fitting with applications to image analysis and automated cartography," *Graphics and Image Processing*, vol. 24, no. 6, pp. 381–395, 1981.

[12] T. Tuytelaars and K. Mikolajczyk, "Local invariant feature detectors: A survey," *Foundations and Trends in Computer Graphics and Vision*, vol. 3, no. 3, pp. 177–280, 2007.

[13] X. Jiang and H. Bunke, "Edge detection in range images based on scan line approximation," *Computer Vision and Image Understanding*, vol. 73, no. 2, pp. 183–199, 1999.

[14] R. O. Duda and P. E. Hart, *Pattern Classification and Scene Analysis*. New York: Wiley, 1972.

[15] K. P. Burnham and D. R. Anderson, *Model Selection and Multimodel Inference: A Practical Information-Theoretic Approach*, 2nd ed. Springer Verlag, 2002, iSBN 0-387-95364-7.

[16] G. Bradski and V. Pisarevsky, "Intel's computer vision library: applications in calibration, stereo segmentation, tracking, gesture, face and object recognition," in *Computer Vision and Pattern Recognition, 2000. Proceedings. IEEE Conference on*, vol. 2, 2000, pp. 796 –797 vol.2.

[17] N. Vaskevicius, A. Birk, K. Pathak, and S. Schwertfeger, "Efficient Representation in 3D Environment Modeling for Planetary Robotic Exploration," *Advanced Robotics*, vol. 24, no. 8-9, pp. 1169–1197, 2010.

[18] L. Di Stefano and A. Bulgarelli, "A simple and efficient connected components labeling algorithm," in *Image Analysis and Processing, 1999. Proceedings. International Conference on*, 1999, pp. 322–327.

[19] N. Vaskevicius, K. Pathak, R. Pascanu, and A. Birk, "Extraction of quadrics from noisy point-clouds using a sensor noise model," in *IEEE International Conference on Robotics and Automation (ICRA)*. IEEE Press, 2010.

[20] B. K. P. Horn, "Closed-form solution of absolute orientation using unit quaternions," *Journal of the Optical Society of America A*, vol. 4, pp. 629–642, 1987.

[21] "Solutions In Perception Challenge ICRA'11." [Online]. Available: http://opencv.willowgarage.com/wiki/SolutionsInPerceptionChallenge

[22] "Robot operating system." [Online]. Available: www.ros.org